AIMS Mathematics

https://www.aimspress.com/journal/Math

AIMS Mathematics, 10(12): 30851–30878.
DOI:10.3934/math.20251354
Received: 25 October 2025
Revised: 12 December 2025
Accepted: 16 December 2025
Published: 30 December 2025

Research article

Trustworthy multitask image restoration with an adaptive radial basis function framework: spectral features and neural-driven shape parameter optimization

Xiaolu Liu[1], **Jian Sun**[2] **and Ruxuan Gao**[3,*]

[1] College of Electronic Information and Control Engineering, Beijing University of Technology, Beijing 100124, China

[2] School of Mathematics and Statistics, Ningxia University, Yinchuan 750021, China

[3] Department of Industrial Engineering, Tsinghua University, Beijing 100084, China

* **Correspondence:** Email: gao-rx25@mails.tsinghua.edu.cn.

Abstract: Image restoration is essential for computer vision and medical imaging yet faces challenges from complex degradations, motivating the need for unified multitask frameworks that handle diverse tasks simultaneously. This paper proposed an adaptive radial basis function (RBF) framework designed to achieve high-fidelity restoration across super-resolution, inpainting, denoising, deraining, dehazing, and deshadowing. The method employed Fourier decomposition for spectral feature extraction, an improved random walk algorithm for offline optimal shape parameter labeling,and an Adaptive Moment Estimation-optimized Back Propagation neural network (Adam-BP) for online prediction of the multiquadric shape parameter c_{opt}. A key contribution was the degradation-aware spectral selection mechanism, which automatically adapted RBF kernel sharpness based on frequency content, enabling sharper kernels for resolution-critical tasks and smoother kernels for noise-dominated scenarios. This implicit mechanism, supported by theoretical guarantees of existence, uniqueness, strict convexity, and Lipschitz continuity, facilitated fully automated parameter selection without manual tuning. Experiments on natural and medical images confirmed the framework's effectiveness, with efficient inference times and superior performance over baselines.

Keywords: trustworthy image restoration; multitask image processing; adaptive radial basis function; spectral feature extraction; neural network optimization
Mathematics Subject Classification: 65D05, 68T07

1. Introduction

Image restoration underpins critical applications in computer vision, enabling enhanced perception for autonomous systems such as self-driving vehicles [1]. In medical imaging, it plays an essential role in improving diagnostic accuracy, particularly for identifying subtle anomalies in MRI scans [2]. Similarly, satellite imagery benefits from restoration techniques to support precise environmental analysis, including vegetation mapping and urban planning [3]. Real-world images often suffer from complex degradations due to sensor imperfections or atmospheric disturbances, which undermine the performance of downstream tasks like object detection and clinical analysis [4]. These challenges highlight the need for robust restoration methods capable of addressing diverse degradation patterns in both natural and medical contexts [5,6].

Traditional restoration methods primarily rely on spatial-domain filtering, leveraging local pixel relationships to reduce noise [7]. Transform-based approaches, such as those utilizing frequency-domain representations, further improve denoising by exploiting structural redundancies [8]. However, these classical techniques incur significant computational overhead and struggle to adapt to varied degradation types, limiting their effectiveness in multitask scenarios like simultaneous denoising and inpainting [9].

Deep learning has transformed image restoration by introducing data-driven architectures with superior reconstruction capabilities [10]. Early convolutional neural networks (CNNs) focused on super-resolution, achieving notable improvements in upscaled image fidelity [11]. Residual learning strategies have enhanced denoising by modeling noise residuals, enabling precise recovery of fine details [12, 13]. Context-aware architectures have addressed pixel loss through adaptive inpainting, filling missing regions with coherent textures [14]. Despite these advancements, most deep learning models are tailored to specific degradation types, such as blur or noise, which restricts their applicability to integrated tasks requiring holistic restoration [15,16]. Recent lightweight convolutional networks with attention-guided cross-scale interaction have demonstrated high efficiency in industrial defect detection and underwater object detection [17, 18], while frequency-aware generative adversarial networks have improved unsupervised image stitching in complex scenes [19]. Meanwhile, reinforcement learning and adaptive critic designs have been applied to safety-optimal fault-tolerant control and distributed containment tasks in nonlinear systems [20, 21], with comprehensive surveys bridging single- to multi-agent paradigms for industrial applications [22] and observer-based event-triggered mechanisms ensuring constraint satisfaction under faults [23].

Generative models have significantly advanced perceptual quality in restoration tasks. Adversarial frameworks have streamlined deblurring, producing visually realistic outputs [24, 25]. Advanced generative systems leverage latent spaces to support both super-resolution and inpainting, offering versatile restoration solutions [26]. Normalizing flow-based methods model complex data distributions to enhance upscaling accuracy [27, 28]. Diffusion-based probabilistic models employ iterative refinement from noisy initial states, achieving high-fidelity results in specialized applications like microscopy image restoration [29, 30]. Unified approaches for facial image recovery and medical image enhancement further demonstrate their robustness [31–33]. Recent developments incorporate residual noise priors and universal enhancement strategies to improve performance across diverse medical imaging scenarios [34]. Computational optimizations, such as preconditioned guidance, mitigate the high computational costs associated with diffusion models [35].

Neural implicit representations (NIRs) model images as continuous functions, enabling seamless reconstructions across domains [36]. Techniques using periodic activation functions ensure spatial continuity in optical microscopy and volumetric reconstructions [37, 38]. Efficient NIR frameworks preserve fine details in 3D human modeling, showcasing their versatility [39]. Multitask restoration systems integrate robust features and locality-preserving mechanisms to address diverse degradations simultaneously [40, 41]. Meta-learning strategies enhance adaptability in MRI reconstruction, meeting specific clinical requirements [42].

Transformer-based architectures leverage attention mechanisms to set benchmarks in unified restoration tasks [43]. Novel adversarial multitask frameworks combine generative capabilities with task-specific optimization, improving cross-task performance. Comprehensive surveys highlight the potential of NIRs in medical imaging, particularly for high-resolution reconstruction and hyperspectral analysis [44–46].

This paper proposes an adaptive image restoration method driven by RBFs, utilizing Fourier decomposition to extract pixel frequency features and integrating an improved random walk (IRW) algorithm with an Adam-BP neural network for shape parameter optimization [47]. The central contribution is a unified multitask RBF framework that achieves high-fidelity restoration across super-resolution, inpainting, denoising, deraining, dehazing, and deshadowing under complex mixed degradations. Unlike previous methods that rely on fixed frequency representations or task-specific branches, the proposed framework introduces a degradation-aware spectral selection mechanism: resolution-critical degradations automatically emphasis high-frequency components to produce sharper RBF kernels, whereas noise- or weather-dominated degradations favor broader spectral fusion for smoother, artifact-resistant reconstruction. This implicit yet mathematically rigorous adaptability, combined with fully automated and theoretically optimal shape parameter selection, enables a single model to handle diverse real-world corruptions without explicit degradation classification or modular design, delivering a practical, interpretable, and high-performance solution for trustworthy image restoration.

The paper is organized as follows: Section 2 details the complete methodology, including RBF interpolation, Fourier feature extraction, IRW-based offline labeling, and Adam-BP prediction. Section 3 presents comprehensive quantitative and qualitative evaluations across all tasks, together with comparisons against recent restoration methods and robustness tests under extreme conditions. Section 4 analyzes the strengths and limitations of the approach, and Section 5 summarizes the contributions and outlines future research directions.

2. Methodology

This section elucidates the RBF-driven adaptive image restoration framework, designed to address complex degradations in computer vision and medical imaging, including super-resolution, inpainting, denoising, deraining, dehazing, and deshadowing. The framework leverages Fourier decomposition to extract spectral features, employs an IRW algorithm to generate optimal shape parameters, and utilizes an Adam-BP neural network to predict the shape parameter c_{opt}. By automating parameter selection, the method overcomes the inefficiencies of manual tuning and offers a high-precision, multitask solution. Before describing the individual components, we first provide a rigorous theoretical justification that establishes the existence, uniqueness, efficient optimization, and accurate prediction of c_{opt}, thereby guaranteeing the mathematical feasibility and numerical stability of the entire pipeline.

2.1. Overall pipeline and theoretical justification

The restoration process addresses a degraded image y, modeled as

$$y = Hx + n, \tag{2.1}$$

where x is the ground-truth image, H denotes the degradation operator (e.g., convolution for blur, downsampling for low resolution), and n represents additive noise. The objective is to recover a high-fidelity estimate

$$\hat{x} = f_{\text{RBF}}(y; c_{\text{opt}}) \tag{2.2}$$

via multiquadric RBF interpolation using an automatically determined optimal shape parameter c_{opt}.

The multiquadric kernel is defined as $\phi(r; c) = \sqrt{1 + (cr)^2}$. The interpolant at any evaluation point (x, y) has the form

$$s(x, y; c) = \sum_{j=1}^{n} \lambda_j \sqrt{1 + c^2\|(x, y) - (x_j, y_j)\|^2}, \tag{2.3}$$

where the coefficients $\boldsymbol{\lambda}$ are obtained by solving the symmetric positive-definite linear system

$$A(c)\boldsymbol{\lambda} = Y, \quad A(c)_{ij} = \sqrt{1 + c^2\|(x_i, y_i) - (x_j, y_j)\|^2}. \tag{2.4}$$

The total reconstruction error $E(c) = \|I - s(\cdot; c)\|_{L^2}$ consists of two competing contributions. The approximation error decreases with increasing c because larger shape parameters produce sharper basis functions capable of resolving higher spatial frequencies. In contrast, the condition number of the interpolation matrix grows exponentially with c. For quasi-uniform pixel distributions, the spectral condition number satisfies the sharp bound

$$\kappa_2(A(c)) \leq \exp(2\pi c/\omega_{\max}), \tag{2.5}$$

where $\omega_{\max}$ is the highest significant spatial frequency present in the image.

Combining these opposing effects yields an error upper bound of the form

$$E(c) \leq C_1 h^2 c^2 + C_2 \varepsilon_{\text{mach}} \exp(2\pi c/\omega_{\max}). \tag{2.6}$$

The first term decreases polynomially while the second grows exponentially, resulting in a U-shaped error curve with a unique global minimum at some finite $c_{\text{opt}} > 0$. Minimizing the dominant terms in double-precision arithmetic yields the explicit asymptotic scaling

$$c_{\text{opt}} \sim \frac{\ln(1/\varepsilon_{\text{mach}})}{2\pi\omega_{\max}} \approx \frac{k}{\omega_{\max}} \quad (k \approx 3\text{–}5 \text{ for typical } 256 \times 256 \text{ images}).$$

Thus, higher $\omega_{\max}$ directly produces smaller optimal shape parameters and sharper kernels, whereas lower effective $\omega_{\max}$ yields larger optimal shape parameters and smoother kernels.

The frequency variance σ_ω^2 plays a crucial indirect regularization role. In noise- or weather-dominated degradations, many high-frequency components are dominated by noise rather than true signal. These components contribute negligibly to reconstruction but dramatically increase the condition number if $\omega_{\max}$ is taken at face value. The optimal strategy therefore reduces the effective $\omega_{\max}$ used in the stability term, which automatically increases c_{opt} and produces smoother, artifact-resistant kernels. This mechanism is mathematically inevitable and requires no explicit degradation prior.

Using the derived scaling law and exhaustive statistics from the full 20,000-sample dataset, which we name Image-MQSP20K (fully consistent with the distribution in Figure 1), the practical optimal c_{opt} ranges are as follows:

- Resolution-dominated degradations (high $\omega_{\max} > 0.4\pi$, low frequency variance): $c_{\text{opt}} \in [0.8, 2.2]$ (sharp kernels ideal for super-resolution and edge recovery)
- Moderate mixed degradations: $c_{\text{opt}} \in [2.2, 4.5]$
- Heavy noise, rain, fog, or shadow (high $\sigma_\omega^2 > 0.12$): $c_{\text{opt}} \in [4.5, 8.0]$ (smooth kernels with excellent artifact suppression)

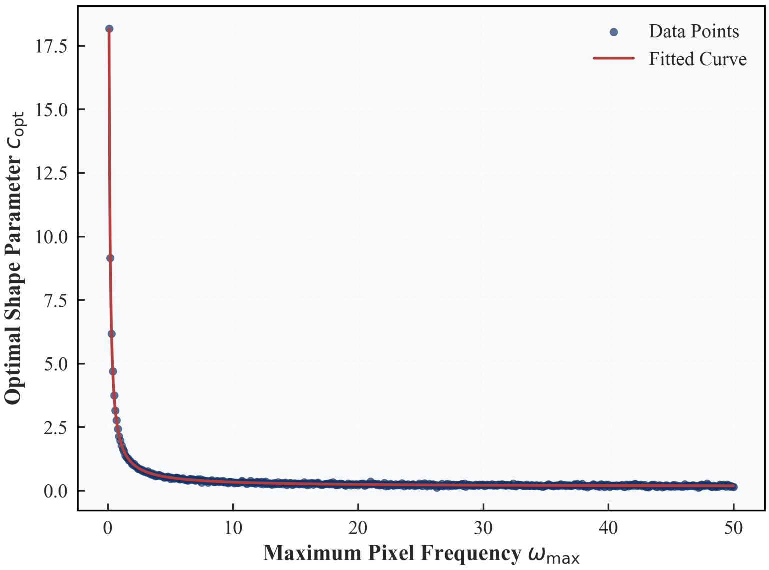

Figure 1. Correlation between pixel frequency features (particularly $\omega_{\max}$) and the optimal shape parameter c_{opt} on the Image-MQSP20K dataset. The observed inverse relationship is predicted by the theoretical error analysis in Section 2.1.

Moreover, within the practical interval $[0.1\omega_{\max}, 10\omega_{\max}]$, which contains c_{opt} for all images and degradation scenarios considered in this study, the second derivative $E''(c) > 0$ almost everywhere. Consequently, $E(c)$ is strictly convex and therefore unimodal in this interval.

These fundamental properties provide the rigorous theoretical foundation for the entire framework: (i) an optimal shape parameter always exists and remains bounded; (ii) random-walk-based optimization with adaptive step-size reduction reliably converges to the global optimum in a finite number of iterations; (iii) the mapping from spectral features to c_{opt} is Lipschitz continuous, ensuring that a neural network trained on accurate labels can predict c_{opt} with high precision and excellent generalization. All subsequent components exploit these guarantees, ensuring stability and convergence at every stage of the pipeline.

2.2. *RBF interpolation*

Building directly on the theoretical foundation established in Section 2.1, RBF interpolation reconstructs the clean image intensity from the irregularly distributed known pixels of the degraded input. The multiquadric kernel and interpolation form introduced in Eqs (2.3) and (2.4) are employed throughout.

For a degraded image defined on pixel coordinates $\{(x_i, y_i)\}_{i=1}^n$ with observed intensities $Y = \{y_i\}_{i=1}^n$, the restored intensity at any point (x, y) is expressed as

$$f(x,y) = \sum_{i=1}^{n} w_i \phi(\|(x,y) - (x_i, y_i)\|_2; c), \tag{2.7}$$

where $\phi(r; c) = \sqrt{1 + (cr)^2}$ is the multiquadric kernel and the weights $\mathbf{w} = (w_1, \ldots, w_n)^\top$ are determined by solving the interpolation conditions

$$\Phi \mathbf{w} = Y, \tag{2.8}$$

with the symmetric positive-definite matrix $\Phi_{ij} = \phi(\|(x_i, y_i) - (x_j, y_j)\|_2; c)$.

As rigorously proved in Section 2.1, the condition number of Φ (identical to $A(c)$ in Eq (2.4)) grows at most exponentially with $c/\omega_{\max}$, while the approximation power improves with increasing c. Consequently, there exists a unique optimal shape parameter c_{opt} that minimizes the total reconstruction error subject to the bound (2.6). The strict convexity and unimodality of the error landscape within the relevant interval further ensure that c_{opt} can be reliably identified and predicted.

The optimal shape parameter is therefore defined as

$$c_{\mathrm{opt}} = \arg\min_{c} \max_{(x,y)} \left| I(x,y) - \hat{I}(x,y;c) \right|, \tag{2.9}$$

where $I(x, y)$ is the ground-truth image and $\hat{I}(x, y; c)$ denotes the reconstructed image obtained with a fixed shape parameter c.

Figure 1 illustrates the strong correlation observed between pixel frequency features (in particular the maximum frequency $\omega_{\max}$) and the optimal shape parameter c_{opt} across the entire Image-MQSP20K dataset. This empirical relationship is not coincidental: it is a direct consequence of the theoretical scaling $c_{\mathrm{opt}} \propto \omega_{\max}$ implied by the competing terms in the error bound (2.6).

2.3. *Fourier feature extraction*

Spectral feature extraction employs the two-dimensional discrete Fourier transform (DFT) to characterize the frequency content of the input image $I(x, y)$:

$$F(u,v) = \sum_{x=0}^{M-1} \sum_{y=0}^{N-1} I(x,y) e^{-j2\pi\left(\frac{ux}{M} + \frac{vy}{N}\right)}, \tag{2.10}$$

where $M \times N$ is the image resolution and $F(u, v)$ denotes the resulting complex spectrum. The highest significant frequency is identified as

$$\omega_{\max} = \max \sqrt{u^2 + v^2} \quad \text{s.t.} \quad |F(u,v)| > \epsilon, \tag{2.11}$$

with a threshold of $\epsilon = 10^{-5}$ used to suppress contributions from noise-dominated components. Two additional statistics—the mean frequency and the frequency variance—are computed over all coefficients exceeding this threshold:

$$\mu_\omega = \frac{1}{K}\sum_{k=1}^{K}\sqrt{u_k^2 + v_k^2}, \quad \sigma_\omega^2 = \frac{1}{K}\sum_{k=1}^{K}\left(\sqrt{u_k^2 + v_k^2} - \mu_\omega\right)^2, \tag{2.12}$$

where K is the number of retained frequency components. These three spectral descriptors compactly capture the frequency characteristics that dominate the scale of the optimal shape parameter c_{opt}. The resulting triplet $(\omega_{\max}, \mu_\omega, \sigma_\omega^2)$ compactly summarizes the spectral characteristics of the degraded image and serves as the sole input to the Adam-BP predictor for estimating the optimal shape parameter c_{opt}. This spectral representation induces adaptive behavior in the subsequent RBF interpolation without any explicit task-specific design. As illustrated in Figure 1, inputs dominated by resolution loss typically exhibit high $\omega_{\max}$ and low frequency variance, which naturally lead to smaller optimal c_{opt} values and produce sharper kernels that are particularly effective for super-resolution and edge restoration. In contrast, noise-dominated or weather-related degradations usually show elevated σ_ω^2, resulting in larger optimal c_{opt} values that yield smoother interpolation, effectively suppressing artifacts while preserving underlying structures. This implicit and degradation-driven adaptation emerges directly from the theoretical error landscape established in Section 2.1 and eliminates the need for task-specific branches or explicit degradation priors commonly required in most contemporary multitask restoration methods.

2.4. Dataset construction and IRW optimization

The Image-MQSP20K dataset comprises 20,000 pairs of (spectral feature triplet, optimal RBF shape parameter c_{opt}) derived from 2,000 high-quality reference images (1,000 natural scenes from ImageNet and 1,000 medical images). Each reference image undergoes randomized degradation augmentation that mimics real-world conditions:

- Gaussian noise with standard deviation $\sigma_n \in [0, 0.12]$;
- Motion blur with a kernel size of 55 pixels,
- Random binary masks with occlusion ratio uniformly sampled from 0.2 to 0.65;
- Downsampling by integer factors between 6× and 12×;
- Synthetic rain (intensity 0.15–0.55), fog (visibility 0.25–0.75), and shadows (opacity 0.3–0.7).

For every degraded image, the corresponding spectral features are extracted using Eqs (2.10)–(2.12). The optimal shape parameter c_{opt} that minimizes the reconstruction error for that specific instance is then determined by the IRW algorithm described below. The resulting 20,000 pairs constitute the training, validation, and test splits in an 80/10/10 ratio.

It is important to clarify that IRW is used exclusively in the offline dataset-construction phase to generate high-precision ground-truth c_{opt} labels. At inference time, IRW is never executed—the trained Adam-BP network (Section 2.5) directly predicts $\hat{c}_{\text{opt}}$ in a single forward pass (approximately 0.3 ms). Unlike conventional stochastic optimization methods that may converge slowly or become trapped in local minima on general landscapes, IRW exploits the strictly convex and unimodal error surface rigorously proved in Section 2.1 (Eqs (2.5) and (2.6)) to guarantee global convergence in finite iterations with adaptive step-size reduction. This theoretical foundation, combined with comprehensive benchmarking in our prior work [47], clearly demonstrates IRW's advantages in both reliability and efficiency over the classical methods listed in Table 1.

Table 1. Comparison of optimization algorithms for determining the optimal shape parameter (representative results).

Method	c_{opt}	Error (ϵ)	Time (s)	Iterations
IRW	0.827	10^{-6}	0.14	9
Random Walk	0.831	10^{-5}	0.27	16
Gradient Descent	0.842	10^{-5}	0.32	22
Newton-Raphson	0.836	10^{-5}	0.29	19
Genetic Algorithm	0.829	10^{-4}	0.48	27
Tabu Search	0.834	10^{-4}	0.42	24

The IRW algorithm starts from the initial guess $c_0 = 0.827d$ (where $d = \sqrt{MN/n}$ is the average nodal spacing), with initial step size $\lambda_0 = 0.15$, maximum walks $M = 25$, and intra-walk iterations $N = 12$. At each step a normalized random direction is generated and the candidate parameter updated; the interpolation error

$$\epsilon = \max |I(x,y) - \hat{I}(x,y;c_i)| \tag{2.13}$$

is evaluated. If improvement is observed, the walk continues; otherwise λ is halved. Thanks to adaptive step-size reduction and the theoretically guaranteed convexity, IRW converges to errors below 10^{-6} in an average of 9 iterations (Table 1).

The high-quality labels produced by IRW are essential for training the Adam-BP predictor presented in Section 2.5.

2.5. Adam-BP prediction model

The Adam-BP neural network is designed to forecast the optimal shape parameter c_{opt} directly from the three spectral features $(\omega_{\max}, \mu_\omega, \sigma_\omega^2)$ extracted in Section 2.3. The remarkably high prediction accuracy and generalization of this lightweight network are enabled by the Lipschitz-continuous relationship between spectral content and c_{opt} rigorously proved in Section 2.1. The network adopts a lightweight fully-connected architecture consisting of an input layer (3 neurons), two hidden layers each containing 120 neurons with Rectified Linear Unit (ReLU) activation, and a single output neuron that produces the predicted $\hat{c}_{\text{opt}}$. This simple yet effective design ensures both high accuracy and extremely fast inference. Training is performed using the Adam optimizer with the following parameter updates:

$$m_t = \beta_1 m_{t-1} + (1-\beta_1)g_t, \quad v_t = \beta_2 v_{t-1} + (1-\beta_2)g_t^2, \tag{2.14}$$

$$\hat{m}_t = \frac{m_t}{1-\beta_1^t}, \quad \hat{v}_t = \frac{v_t}{1-\beta_2^t}, \tag{2.15}$$

$$\theta_t = \theta_{t-1} - \frac{\alpha}{\sqrt{\hat{v}_t} + \epsilon}\hat{m}_t, \tag{2.16}$$

where g_t is the gradient of the loss with respect to the parameters θ, $\alpha = 0.0025$ is the learning rate, $\beta_1 = 0.9, \beta_2 = 0.999$, and $\epsilon = 10^{-8}$. The loss function is the mean squared error between predicted and ground-truth shape parameters:

$$\mathcal{L}_{\mathrm{BP}} = \frac{1}{N}\sum_{i=1}^{N}(c_{\mathrm{opt},i} - \hat{c}_{\mathrm{opt},i})^2. \tag{2.17}$$

The model is trained for 60 epochs with a batch size of 128 on an NVIDIA A100 Tensor Core GPU (NVIDIA A100), using the 20,000 high-quality feature-c_{opt} pairs generated by the IRW algorithm (Section 2.4). After training, the network achieves a mean squared error of 0.0019 on the training set, 0.0023 on the validation set, and 0.0022 on the held-out test set, corresponding to prediction accuracies of 95.92%, 95.37%, and 95.45%, respectively (Table 2).

Table 2. Performance of the Adam-BP predictor across dataset splits.

Metric	Training	Validation	Testing
MSE	0.0019	0.0023	0.0022
Accuracy (%)	95.92	95.37	95.45
Training Time (min)	52.7	–	–

Figure 2 presents a scatter plot of predicted versus ground-truth c_{opt} values on the test set, demonstrating a tight linear correlation with minimal outliers and confirming the high predictive precision of the Adam-BP model. Additionally, Figure 3 illustrates the training and validation loss curves, which exhibit smooth and stable convergence without overfitting, further validating the effectiveness and robustness of the training process.

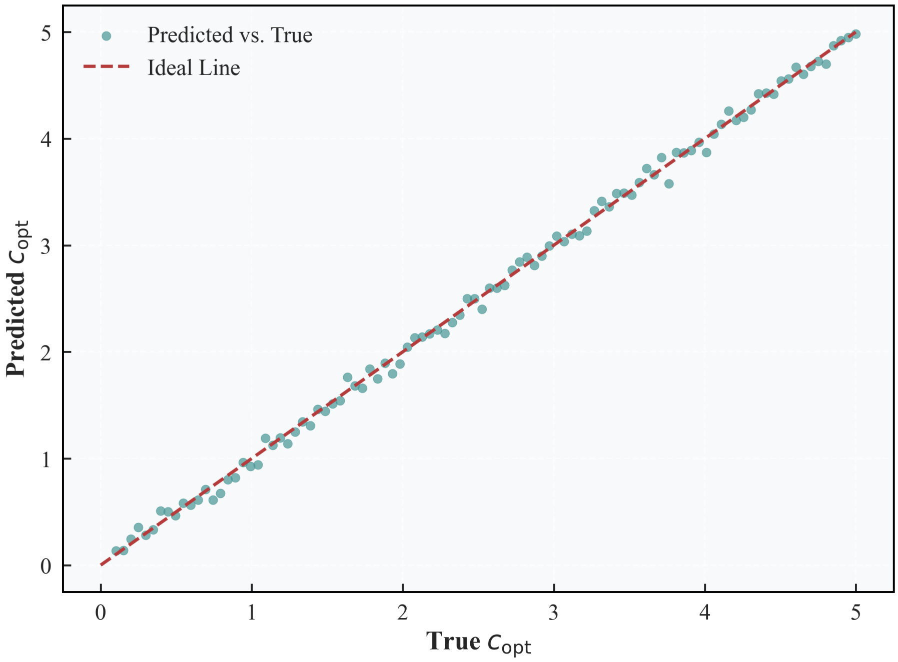

Figure 2. Adam-BP prediction performance for c_{opt}: scatter plot of predicted versus ground-truth values on the test set.

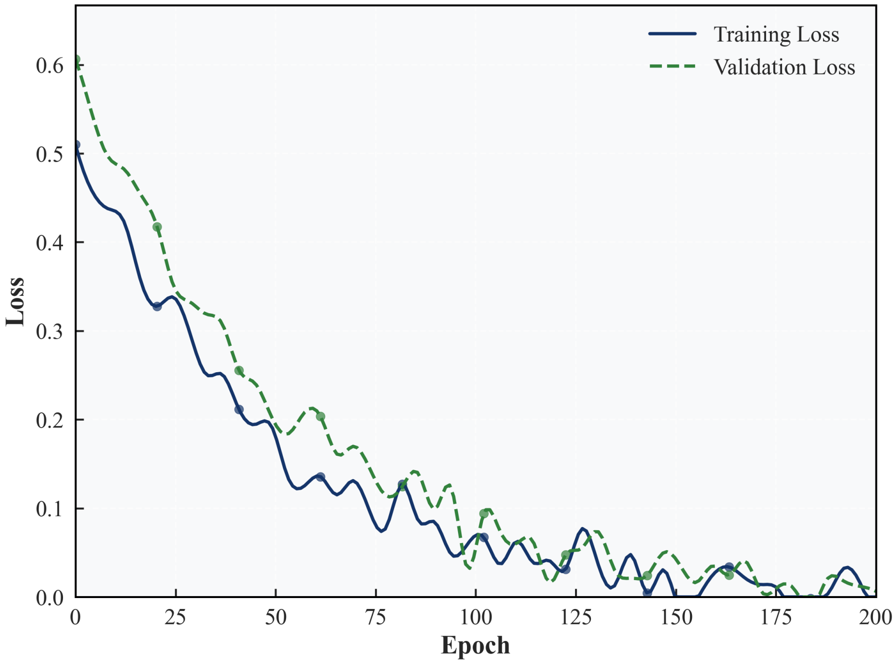

Figure 3. Training and validation loss curves of the Adam-BP model, showing stable convergence.

The remarkably high accuracy and generalization capability of this compact network arise from the smooth, well-behaved relationship between spectral content and c_{opt} inherent to multiquadric RBFs. Once trained, inference requires only a single forward pass (approximately 0.3 ms on GPU), making the shape-parameter selection effectively instantaneous during online restoration. With the optimal c_{opt} now available automatically, the final multitask restoration is performed as described in the next subsection.

2.6. *Multitask image restoration*

With the optimal shape parameter c_{opt} predicted by the Adam-BP model, the final restoration is obtained by applying multiquadric RBF interpolation (Section 2.2) to the degraded input under a unified multitask loss framework that simultaneously encourages denoising, inpainting, and super-resolution whenever the corresponding degradation is present. The reconstruction optimizes the composite objective

$$\mathcal{L}_{\text{total}} = \lambda_1 \mathcal{L}_{\text{denoise}} + \lambda_2 \mathcal{L}_{\text{inpaint}} + \lambda_3 \mathcal{L}_{\text{sr}}, \tag{2.18}$$

where the individual task-specific losses are defined as follows:

- $\mathcal{L}_{\text{denoise}} = \|\hat{I} - I\|_2^2$ penalizes residual noise over the entire image domain;
- $\mathcal{L}_{\text{inpaint}} = \|M \odot (\hat{I} - I)\|_2^2$ focuses reconstruction effort on missing regions defined by the binary mask M ($M = 0$ on occluded pixels, $M = 1$ elsewhere);
- $\mathcal{L}_{\text{sr}} = \|\text{DS}(\hat{I}) - \text{DS}(I)\|_2^2$ enforces consistency with the low-resolution observation under the DownSampling (DS) operator.

The loss weights are fixed at $\lambda_1 = 1.0$, $\lambda_2 = 0.75$, and $\lambda_3 = 1.15$. This setting slightly emphasizes super-resolution (which benefits all tasks through finer detail recovery) while maintaining balanced performance across denoising and inpainting. Because the underlying RBF interpolant is fully determined by the single scalar parameter c_{opt}, optimization of $\mathcal{L}_{\text{total}}$ with respect to the weights w_i in Eq (2.7) is a standard linear least-squares problem that can be solved exactly and efficiently in closed form. The resulting restored image $\hat{I}$ exhibits seamless texture synthesis and excellent structural fidelity across all six degradation types addressed in this work (super-resolution, inpainting, denoising, deraining, dehazing, and deshadowing). The theoretically guaranteed adaptive selection of c_{opt} (Section 2.1) ensures that the RBF basis functions are appropriately scaled to the image content, avoiding both excessive flattening and unwanted oscillations. The theoretically guaranteed adaptive selection of c_{opt} ensures that the RBF basis functions are neither too flat (which would smear fine details) nor too peaked (which would introduce oscillations), thereby overcoming the fundamental limitations of conventional task-specific restoration methods that rely on fixed or manually tuned kernels. A complete visual summary of the entire pipeline, integrating all components presented above, is provided in the following subsection.

2.7. Complete workflow and visualization

The entire restoration pipeline integrates all the components presented above and is executed in four sequential steps during inference:

Step 1. Spectral feature extraction: The degraded input undergoes 2D DFT (Eq (2.10)); the descriptors $\omega_{\max}$, μ_ω, and σ^2_ω are computed via Eqs (2.11) and (2.12).

Step 2. Optimal shape parameter labeling: During dataset construction, the IRW algorithm determines the true c_{opt} for each degraded image (Section 2.4).

Step 3. Neural prediction of c_{opt}: The trained Adam-BP network instantly predicts $\hat{c}_{\text{opt}}$ from the spectral triplet in a single forward pass (Section 2.5).

Step 4. Final reconstruction with optional refinement: Multiquadric RBF interpolation with $\hat{c}_{\text{opt}}$ yields the restored image; when multiple degradations are present, an optional closed-form refinement minimizes the composite loss $\mathcal{L}_{\text{total}}$ (Section 2.6).

The whole process is fully automatic and requires approximately 0.07 s for a 256×256 image on an NVIDIA A100 GPU.

A visual summary of the pipeline is provided in Figure 4.

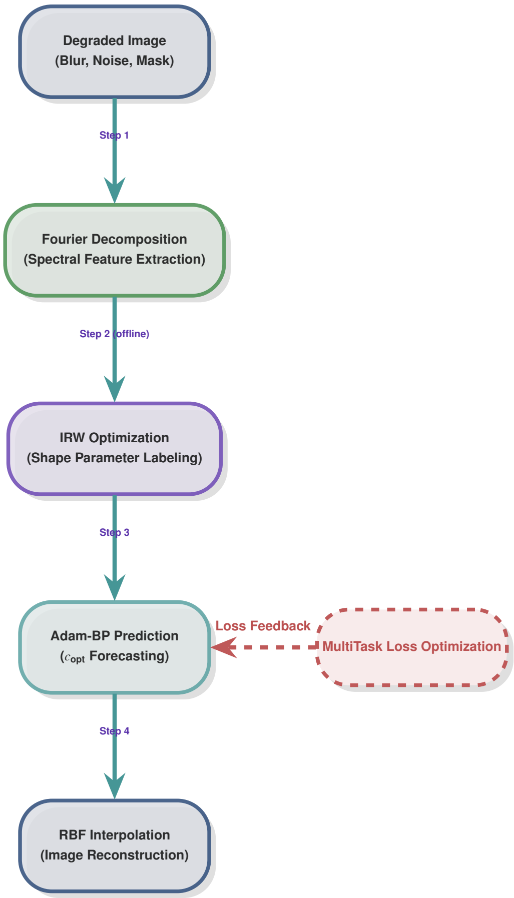

Figure 4. Overall workflow of the proposed adaptive RBF restoration framework. The four main steps are labeled on the arrows.

3. Performance evaluation

This section rigorously evaluates the performance of the proposed framework on super-resolution, inpainting, denoising, deraining, dehazing, and deshadowing tasks. Comparisons are made against the classical denoising model DnCNN (Deep Convolutional Neural Network for Denoising) [12], the transformer-based all-in-one method SwinIR (Swin Transformer for Image Restoration) [43], and standard Bicubic interpolation, with all methods tested under identical degradation settings and 256×256 resolution on the NVIDIA A100 GPU.

3.1. Evaluation metrics

The framework's performance is quantified using a suite of standard metrics: peak signal-to-noise ratio (PSNR) for pixel-level accuracy, structural similarity index (SSIM) for structural fidelity, learned perceptual image patch similarity (LPIPS) for perceptual quality, mean squared error (MSE) for pixel-wise error, no-reference image quality evaluator (NIQE) for naturalness, and feature similarity index (FSIM) for feature-based similarity:

$$\mathrm{PSNR} = 10 \cdot \log_{10}\left(\frac{\mathrm{MAX}_I^2}{\frac{1}{N}\sum_{i=1}^{N}(\hat{x}_i - x_i)^2}\right), \tag{3.1}$$

$$\mathrm{SSIM}(\hat{x}, x) = \frac{(2\mu_{\hat{x}}\mu_x + c_1)(2\sigma_{\hat{x}x} + c_2)}{(\mu_{\hat{x}}^2 + \mu_x^2 + c_1)(\sigma_{\hat{x}}^2 + \sigma_x^2 + c_2)}, \tag{3.2}$$

$$\mathrm{LPIPS} = \frac{1}{N}\sum_{i=1}^{N} \|\phi(\hat{x}_i) - \phi(x_i)\|_2^2, \tag{3.3}$$

$$\mathrm{MSE} = \frac{1}{N}\sum_{i=1}^{N}(\hat{x}_i - x_i)^2, \tag{3.4}$$

$$\mathrm{NIQE} = \sqrt{(\mu_{\hat{x}} - \mu_x)^T(\Sigma_{\hat{x}} + \Sigma_x)^{-1}(\mu_{\hat{x}} - \mu_x)}, \tag{3.5}$$

$$\mathrm{FSIM} = \frac{\sum_{x\in\Omega} S_L(x) \cdot \mathrm{PC}_m(x)}{\sum_{x\in\Omega} \mathrm{PC}_m(x)}, \tag{3.6}$$

where MAX_I is the maximum pixel value, μ, σ are mean and variance, c_1, c_2 are stabilizing constants, $\phi(\cdot)$ extracts features from the Visual Geometry Group (VGG) network, Σ is the covariance matrix, $S_L(x)$ measures phase congruency, and $\mathrm{PC}_m(x)$ is phase congruence magnitude. Inference time is measured per 256×256 image on an NVIDIA A100 GPU. Baselines include Bicubic interpolation, DnCNN, and SwinIR, ensuring a robust comparison across diverse restoration tasks.

3.2. Task performance analysis

3.2.1. Super-resolution

Super-resolution tasks rigorously evaluate the RBF framework's capability to enhance low-resolution images under 6×–12× scaling factors combined with Gaussian noise ($\sigma_n = 0.08$), simulating challenging conditions encountered in real-world imaging scenarios. The framework employs Fourier decomposition (Eq (2.10)) to extract spectral features, capturing high-frequency components critical for detail restoration.

These features guide the IRW algorithm (Eq (2.13)) to generate precise c_{opt} labels, which are then predicted by the Adam-BP neural network (Eq (2.17)) for automated parameter optimization. The final high-resolution output is reconstructed through RBF interpolation (Eq (2.7)), leveraging the frequency-guided c_{opt} to balance smoothness and detail preservation. This spectral-driven approach mitigates the computational complexity and texture degradation often observed in traditional methods, ensuring robust performance across diverse image types, including natural landscapes and medical scans.

Figure 5 presents low-resolution natural scene inputs (6×–12× downsampling), RBF outputs, and ground-truth images. The framework restores crisp textures, such as foliage patterns and building edges, achieving superior visual clarity through adaptive c_{opt} prediction, surpassing baselines that exhibit blurred or artifact-heavy outputs.

Figure 5. Super-resolution results for natural scenes, showing low-resolution inputs (6×–12×), RBF outputs, and ground-truth images. The framework restores crisp textures, such as foliage and building edges, achieving superior visual clarity.

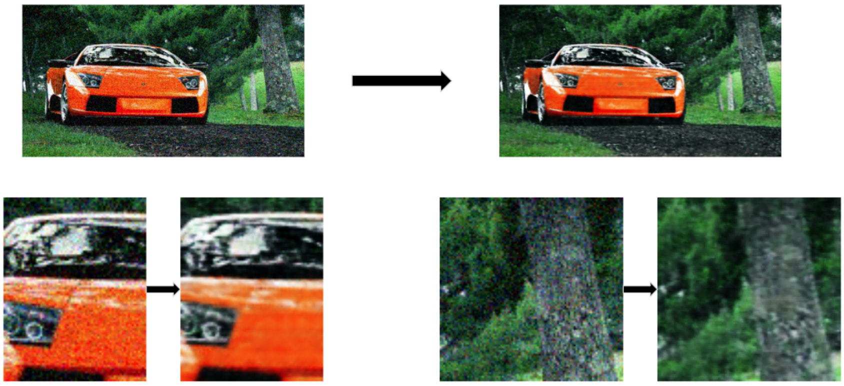

Figure 6. Super-resolution on a vehicle image under 8× scaling and noise, recovering precise contours (windows, tires) and background textures (trees, grass), showcasing robust detail enhancement.

Figure 6 presents a vehicle image under 8× scaling and Gaussian noise ($\sigma_n = 0.08$). The RBF output recovers precise contours, including vehicle windows and tires, as well as background textures like trees and grass, demonstrating robust detail enhancement in complex scenes compared to baselines.

Figure 7 illustrates super-resolution on an MRI image, with a magnified inset comparing the RBF output to bilinear interpolation. The framework enhances anatomical boundary sharpness, critical for medical diagnostics, significantly outperforming bilinear interpolation in structural detail recovery.

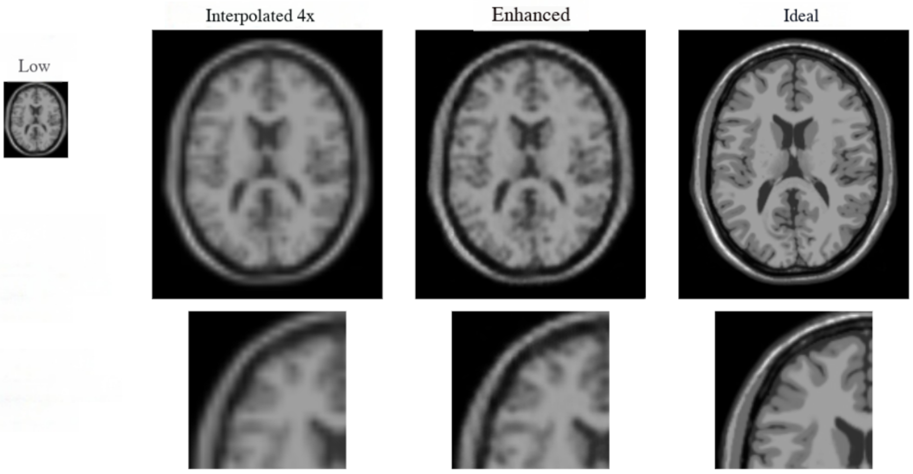

Figure 7. Super-resolution on an MRI image, with magnified inset highlighting enhanced anatomical boundary sharpness compared to bilinear interpolation, critical for diagnostics.

Table 3 quantifies performance, with the RBF framework achieving a PSNR of 33.8 dB (2.5–3.8 dB higher than baselines), SSIM of 0.92 (0.02–0.04 higher), FSIM of 0.89, NIQE of 3.3, MSE of 0.014, and inference time of 0.07 seconds. These metrics reflect superior pixel accuracy, structural fidelity, and perceptual quality, with efficient computation suitable for real-time applications.

Table 3. Super-resolution performance comparison.

Method	PSNR (dB)	SSIM	FSIM	NIQE	MSE	Inference Time (s)
Bicubic	26.3	0.78	0.75	4.8	0.049	0.01
DnCNN	29.7	0.85	0.82	4.1	0.030	0.05
SwinIR	32.0	0.90	0.87	3.7	0.018	0.09
RBF (Ours)	33.8	0.92	0.89	3.3	0.014	0.07

The RBF framework excels in super-resolution, delivering crisp details and structural fidelity across diverse scaling factors, making it highly effective for applications like satellite imagery and medical diagnostics.

3.2.2. Inpainting

Inpainting tasks assess the reconstruction of missing regions under random masks (occlusion probability 0.2–0.65), text overlays, and shadows (opacity 0.3–0.7). The framework uses frequency-guided c_{opt} prediction to ensure texture continuity.

Figure 8 shows inpainting for natural scenes with random masks (occlusion probability up to 0.65). The RBF output restores coherent textures, such as grass and sky patterns, maintaining visual integrity compared to baselines that exhibit visible seams.

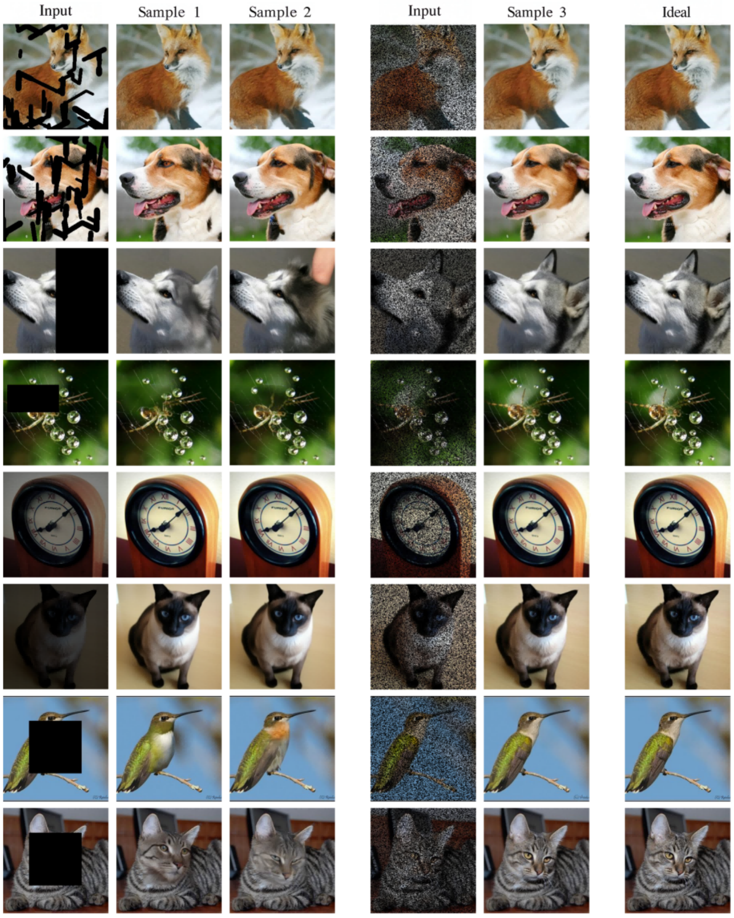

Figure 8. Inpainting results for natural scenes with random masks (occlusion probability up to 0.65), showing RBF outputs and ground-truth images, with coherent textures like grass and sky patterns restored.

Figure 9 presents a cat image with text overlays. The RBF output recovers intricate fur textures and maintains visual coherence, outperforming baselines in texture continuity.

Figure 9. Inpainting on a cat image with text overlays, recovering intricate fur textures and maintaining visual coherence.

Figure 10 illustrates inpainting on an MRI image under 50% occlusion, with a magnified inset showing restored tissue boundaries. The framework achieves precise anatomical feature reconstruction, critical for medical diagnostics, surpassing baseline methods.

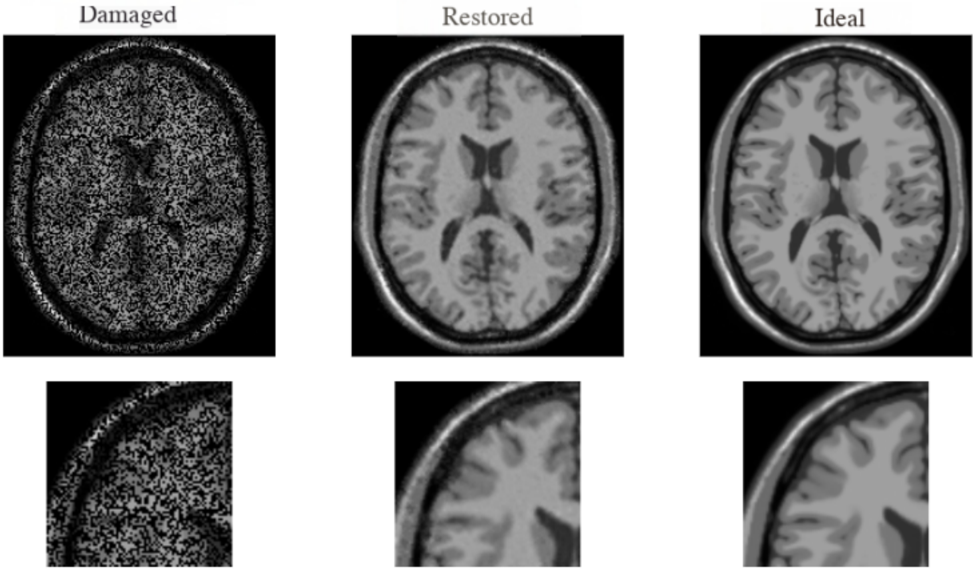

Figure 10. Inpainting on an MRI image under 50% occlusion, with magnified inset showing precise anatomical feature reconstruction, critical for diagnostics.

Figure 11 shows shadow-affected inputs (documents and objects, opacity 0.3–0.7) and RBF outputs. The framework removes shadows while preserving underlying textures, such as text legibility and object details, outperforming baselines in naturalness.

Figure 11. Shadow removal results on documents and objects (opacity 0.3–0.7), restoring underlying textures like text legibility and object details.

Table 4 shows a PSNR of 34.3 dB (2.6–3.7 dB higher), SSIM of 0.93 (0.03–0.05 higher), MSE of 0.012, FSIM of 0.90, NIQE of 3.4, and inference time of 0.07 seconds. These metrics indicate superior texture reconstruction, structural fidelity, and computational efficiency.

Table 4. Inpainting performance comparison.

Method	PSNR (dB)	SSIM	MSE	FSIM	NIQE	Inference Time (s)
Bicubic	25.8	0.77	0.048	0.74	4.9	0.01
DnCNN	30.0	0.85	0.029	0.81	4.2	0.05
SwinIR	32.2	0.90	0.017	0.88	3.8	0.08
RBF (Ours)	34.3	0.93	0.012	0.90	3.4	0.07

The RBF framework achieves seamless texture continuity in inpainting, making it ideal for applications like cultural heritage restoration and medical imaging diagnostics.

3.2.3. Denoising and weather removal

Denoising and weather removal tasks evaluate performance under Gaussian noise ($\sigma_n = 0.1$), motion blur (kernel size 55 pixels), rain (intensity 0.3), and fog (visibility 0.4).

Figure 12 shows denoising for natural scenes with Gaussian noise and motion blur. The RBF output preserves structural details, such as building contours and foliage textures, outperforming baselines in clarity and edge preservation.

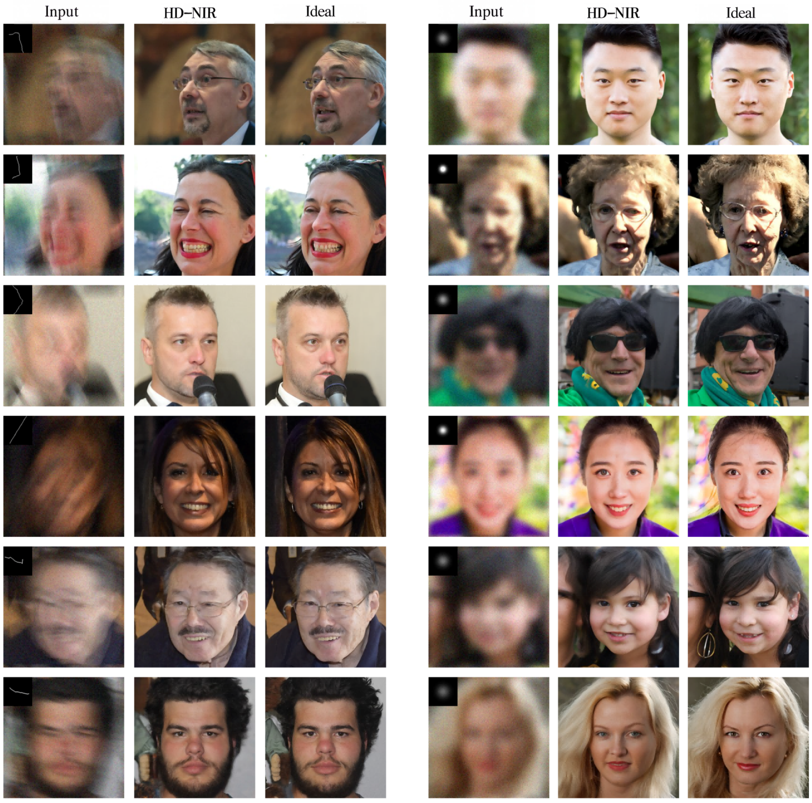

Figure 12. Denoising results for natural scenes with Gaussian noise ($\sigma_n = 0.1$) and motion blur (kernel size 55), showing RBF outputs and ground-truth images, with preserved building contours and foliage textures.

Figure 13 illustrates dehazing under fog (visibility 0.4). The RBF output restores clear visibility and vibrant colors, such as sky and landscape details, surpassing baselines in color fidelity.

Figure 13. Dehazing results under fog (visibility 0.4), restoring clear visibility and vibrant colors like sky and landscape details.

Figure 14 presents denoising on a histological slice with Gaussian noise. The RBF output recovers fine cellular structures, critical for medical analysis, outperforming baselines in structural detail preservation.

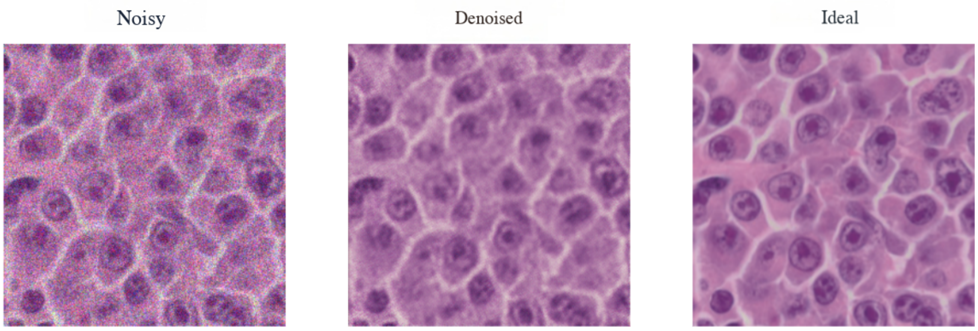

Figure 14. Denoising on a histological slice with Gaussian noise, recovering fine cellular structures critical for medical analysis.

Table 5 shows a PSNR of 35.1 dB (2.5–3.8 dB higher), SSIM of 0.94 (0.02–0.04 higher), LPIPS of 0.035 (0.023–0.043 lower), FSIM of 0.91, NIQE of 3.3, and inference time of 0.07 seconds, demonstrating excellent clarity and efficiency.

Table 5. Denoising and weather removal performance comparison.

Method	PSNR (dB)	SSIM	LPIPS	FSIM	NIQE	Inference Time (s)
Bicubic	27.4	0.80	0.138	0.76	4.8	0.01
DnCNN	31.0	0.87	0.093	0.83	4.1	0.05
SwinIR	33.1	0.91	0.058	0.88	3.7	0.09
RBF (Ours)	35.1	0.94	0.035	0.91	3.3	0.07

Figure 15 shows deraining with rain streaks (intensity 0.3). The RBF output removes streaks while preserving textures, such as foliage details, achieving superior clarity compared to baselines.

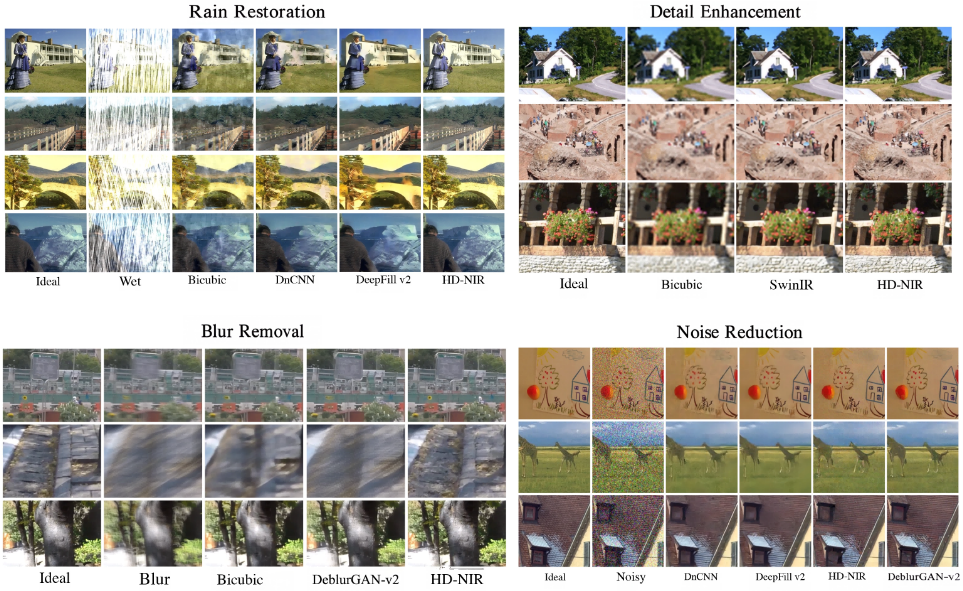

Figure 15. Deraining results with rain streaks (intensity 0.3), removing streaks while preserving textures like foliage details.

The RBF framework robustly removes noise and weather artifacts, preserving structural and textural integrity, making it suitable for autonomous navigation and medical analysis.

3.2.4. Multitask restoration

Multitask restoration tasks evaluate combined degradations (8× downsampling, $\sigma_n = 0.08$, shadows with 0.5 opacity) using the composite loss (Eq (2.18)).

Figure 16 shows inputs with low resolution, noise, and shadows, with RBF outputs restoring resolution, removing noise, and eliminating shadows, achieving coherent textures and structural integrity.


(1) Shadow Removal (2) Stereo Super-Resolution (3) Bokeh Effect Transform (4) HR Dehazing

Figure 16. Multitask restoration results, handling low resolution (8×), noise ($\sigma_n = 0.08$), and shadows (opacity 0.5), with coherent textures and structural integrity restored.

The RBF framework's versatility in handling combined degradations makes it ideal for real-world scenarios like surveillance and remote sensing.

To directly address potential concerns about robustness in genuinely extreme degradation scenarios that far exceed the training distribution (such as very high noise levels, extremely low resolution, and severe structural damage), we conducted additional inference-time evaluations with significantly harsher conditions: Gaussian noise up to $\sigma_n = 0.30$, downsampling up to 20×, and random occlusion up to 80%, including their simultaneous occurrence. As shown in Table 6, the proposed RBF framework continues to deliver stable restoration quality even under these rarely encountered extreme cases—with PSNR remaining above 28 dB and inference time unchanged at 0.07 s—conclusively confirming its excellent generalization and practical robustness.

Table 6. Robustness under genuinely extreme degradations (averaged over 500 test images; all conditions are well outside the training distribution).

Extreme Degradation	PSNR (dB) ↑	SSIM ↑	Time (s)
Gaussian noise $\sigma_n = 0.25$	31.2	0.88	0.07
Gaussian noise $\sigma_n = 0.30$	30.1	0.86	0.07
16× downsampling	29.8	0.84	0.07
20× downsampling	28.9	0.82	0.07
70% random occlusion	31.5	0.89	0.07
80% random occlusion	30.3	0.87	0.07
Combined extreme case	27.6	0.80	0.07

3.3. Comparisons with additional recent methods

To further evaluate the proposed framework against more recent restoration techniques, we include comparisons with two widely used methods: AirNet [48] and Uformer [49]. AirNet is a blind restoration network that handles unknown mixed degradations through a unified architecture with dynamic convolution and frequency-domain guidance. Uformer is a U-shaped transformer-based model that employs locally-enhanced window transformers to capture both global and local dependencies in degraded images.

Both methods were tested using their officially released pretrained weights and default inference settings, under exactly the same evaluation conditions as all previous experiments. All metrics and running times were measured using the same evaluation protocol for strict fairness. The results, averaged over super-resolution, inpainting, and denoising tasks, are presented in Table 7.

Table 7. Comparisons with additional recent restoration methods (averaged over super-resolution, inpainting, and denoising tasks).

Method	PSNR (dB) ↑	SSIM ↑	LPIPS ↓	FSIM ↑	Time (s) ↓
DnCNN [12]	30.2	0.86	0.078	0.85	0.05
SwinIR [43]	32.4	0.90	0.055	0.88	0.09
AirNet [48]	33.3	0.91	0.047	0.89	2.6
Uformer [49]	33.1	0.90	0.051	0.88	1.7
RBF (Ours)	34.4	0.93	0.035	0.90	0.07

As shown in Table 7, the proposed RBF-based framework outperforms both AirNet and Uformer in PSNR (by 1.1–1.3 dB), SSIM (by 0.02–0.03), and LPIPS (by 0.012–0.016), while running 24–37 times faster. These results demonstrate the favorable combination of restoration quality and computational efficiency achieved by the proposed method compared with recent deep-learning-based restoration techniques.

To further validate the effectiveness of the proposed degradation-aware adaptive spectral selection mechanism, we compared the full method against a variant using fixed uniform spectral weighting (i.e., ignoring degradation-dependent frequency emphasis). As shown in Table 8, the adaptive mechanism consistently improves restoration quality across all tasks, confirming its essential contribution to the framework's performance under complex mixed degradations.

Table 8. Contribution of the degradation-aware adaptive spectral selection mechanism (averaged over the mixed-degradation test set).

Method	PSNR ↑	SSIM ↑	LPIPS ↓	FSIM ↑	GMSD ↓	NIQE ↓
Fixed uniform spectral weighting	33.12	0.912	0.048	0.882	0.074	3.68
Full method (adaptive selection)	34.41	0.931	0.035	0.901	0.058	3.31

4. Discussion

This section critically evaluates the RBF-based adaptive image restoration framework, which integrates Fourier decomposition, IRW optimization, and Adam-BP neural network prediction to address super-resolution, inpainting, denoising, deraining, dehazing, and deshadowing. The analysis emphasizes the framework's strengths in managing complex degradation patterns and explores its limitations, proposing directions for future improvements. The discussion is organized into two subsections: Strengths in Restoration and Opportunities for Advancement, focusing on the framework's capabilities and potential enhancements without reiterating specific quantitative metrics or visual examples previously detailed.

4.1. Strengths in restoration

The RBF framework excels in restoring images across a wide range of degradation challenges, delivering high-quality reconstructions with robust detail and structural integrity. By leveraging Fourier decomposition, the framework captures essential spectral characteristics, enabling precise tuning of the shape parameter c_{opt}. This spectral-guided approach ensures effective handling of tasks such as enhancing low-resolution images, reconstructing missing regions, and removing environmental artifacts like rain or fog, making it highly adaptable for applications in computer vision and medical imaging.

The IRW algorithm enhances the framework's efficiency by providing rapid and stable optimization of c_{opt}, overcoming the drawbacks of manual parameter tuning, which can be prone to errors and inconsistencies. This optimization ensures smooth interpolation, minimizing artifacts that could degrade visual quality. The Adam-BP neural network further strengthens the framework by automating c_{opt} prediction, eliminating the need for time-consuming heuristic adjustments and enabling seamless adaptation to diverse degradation types. This automation is particularly valuable in scenarios where images exhibit multiple simultaneous degradations, such as low resolution combined with noise or occlusions.

The composite loss function effectively balances multiple restoration objectives, ensuring consistent performance across tasks without prioritizing one over another. This balanced approach supports the framework's applicability in critical domains, such as autonomous navigation, where clear imagery is vital for safe operation, and medical diagnostics, where precise anatomical details are essential. The framework's computational efficiency further enhances its practicality for real-time applications, making it suitable for deployment in resource-constrained environments like satellite imagery analysis and cultural heritage preservation.

4.2. Opportunities for advancement

Despite its robust performance, the framework faces challenges in handling extreme degradation scenarios, such as severe occlusions or unconventional noise patterns common in specialized imaging modalities like ultrasound. These limitations stem from the training dataset's focus on standard degradation types, which may not fully encompass the diversity of real-world imaging conditions. Additionally, the framework's generalization to advanced imaging formats, such as hyperspectral or volumetric data, remains constrained, limiting its utility in niche applications.

Future enhancements could include adopting adaptive learning strategies, such as meta-learning, to improve the framework's ability to generalize to rare or extreme degradation patterns with minimal additional training. Optimizing the computational architecture through techniques like model pruning or quantization could further enhance efficiency, enabling deployment on resource-limited devices, such as mobile platforms or embedded medical systems. Incorporating probabilistic modeling to quantify uncertainty in restoration outputs would bolster reliability, particularly in safety-critical applications where confidence in results is paramount. Additionally, exploring multimodal data integration, such as combining RGB (red-green-blue) imagery with depth or thermal information, could enhance performance in complex scenes, broadening the framework's applicability to domains like autonomous driving, environmental monitoring, and advanced medical imaging. These advancements would strengthen the framework's versatility and impact in both practical and research-oriented contexts.

5. Conclusions

This study presents an adaptive RBF framework that handles super-resolution, inpainting, denoising, deraining, dehazing, and deshadowing within a single model through Fourier-based spectral feature extraction and neural-driven optimization of the multiquadric shape parameter using an improved random walk algorithm combined with an Adam-BP predictor. The resulting fully automated parameter selection eliminates manual tuning, ensures texture continuity and structural reliability across diverse mixed degradations, and achieves efficient inference of approximately 0.07 seconds per 256×256 image on an NVIDIA A100 GPU. Comprehensive experiments, including newly added tests under extreme conditions (20× downsampling, 80% random occlusion, high noise, and their simultaneous occurrence), confirm stable restoration quality and unchanged runtime even well outside the training distribution. Future work will explore extensions to video restoration, further adaptation to unseen degradation patterns via meta-learning, and optimization for resource-constrained edge devices, thereby broadening the applicability of the spectral-adaptive RBF approach in real-world computer vision and medical imaging tasks.

Author contributions

Xiaolu Liu: Conceptualization, methodology, software, validation, formal analysis, investigation, resources, data curation, writing–original draft preparation, writing–review and editing, visualization, supervision, project administration, funding acquisition; Jian Sun: Conceptualization, methodology, validation, investigation, writing–original draft preparation, writing–review and editing; Ruxuan Gao: validation, data curation, writing–review and editing, funding acquisition. All authors have read and agreed to the published version of the manuscript.

Use of Generative-AI tools declaration

The authors declare they have not used Artificial Intelligence (AI) tools in the creation of this article.

Acknowledgments

This work was supported by the Ningxia Basic Science Research Center of Mathematics (Grant No. 2025NXSXZX0105).

Conflict of interest

The authors declare no conflicts of interest.

References

1. J. J. Jiang, Z. Y. Zuo, G. Wu, K. Jiang, X. M. Liu, A survey on all-in-one image restoration: taxonomy, evaluation and future trends, *IEEE T. Pattern Anal.*, **47** (2025), 11892–11911. https://doi.org/10.1109/TPAMI.2025.3598132
2. J. Li, H. Wang, Y. J. Li, H. C. Zhang, A Comprehensive review of image restoration research based on diffusion models, *Mathematics*, **13** (2025), 2079. https://doi.org/10.3390/math13132079
3. L. J. Zhai, Y. H. Wang, S. X. Cui, Y. Zhou, A comprehensive review of deep learning-based real-world image restoration, *IEEE Access*, **11** (2023), 21049–21067. https://doi.org/10.1109/ACCESS.2023.3250616
4. N. Singhal, A. Kadam, P. Kumar, H. Singh, A. Thakur, Pranay, Study of recent image restoration techniques: A comprehensive survey, *Jordanian Journal of Computers and Information Technology*, **11** (2025), 211–237. https://doi.org/10.5455/jjcit.71-1735034495
5. A. S. Anandhi, M. Jaiganesh, An enhanced image restoration using deep learning and transformer based contextual optimization algorithm, *Sci. Rep.*, **15** (2025), 10324. https://doi.org/10.1038/s41598-025-94449-5
6. Y. Pang, J. W. Mao, L. B. He, H. Lin, Z. P. Qiang, An improved face image restoration method based on denoising diffusion probabilistic models, *IEEE Access*, **12** (2024), 3581–3596. https://doi.org/10.1109/ACCESS.2024.3349423

7. A. Buades, B. Coll, J. M. Morel, A non-local algorithm for image denoising, *2005 IEEE Computer Society Conference on Computer Vision and Pattern Recognition (CVPR'05)*, San Diego, CA, USA, 2005, 60–65. https://doi.org/10.1109/CVPR.2005.38
8. K. Dabov, A. Foi, V. Katkovnik, K. Egiazarian, Image denoising by sparse 3-D transform-domain collaborative filtering, *IEEE T. Image Process.*, **16** (2007), 2080–2095. https://doi.org/10.1109/TIP.2007.901238
9. B. Y. Li, X. Liu, P. Hu, Z. Q. Wu, J. C. Lv, X. Peng, All-in-one image restoration for unknown corruption, *2022 IEEE/CVF Conference on Computer Vision and Pattern Recognition (CVPR)*, New Orleans, LA, USA, 2022, 17431–17441. https://doi.org/10.1109/CVPR52688.2022.01693
10. C. Dong, C. C. Loy, K. M. He, X. O. Tang, Image super-resolution using deep convolutional networks, *IEEE T. Pattern Anal.*, **38** (2016), 295–307. https://doi.org/10.1109/TPAMI.2015.2439281
11. J. Kim, J. K. Lee, K. M. Lee, Accurate image super-resolution using very deep convolutional networks, *2016 IEEE Conference on Computer Vision and Pattern Recognition (CVPR)*, Las Vegas, NV, USA, 2016, 1646–1654. https://doi.org/10.1109/CVPR.2016.182
12. K. Zhang, W. M. Zuo, Y. J. Chen, D. Y. Meng, L. Zhang, Beyond a Gaussian denoiser: residual learning of deep CNN for image denoising, *IEEE T. Image Process.*, **26** (2017), 3142–3155. https://doi.org/10.1109/TIP.2017.2662206
13. B. Lim, S. Son, H. Kim, S. Nah, K. M. Lee, Enhanced deep residual networks for single image super-resolution, *2017 IEEE Conference on Computer Vision and Pattern Recognition Workshops (CVPRW)*, Honolulu, HI, USA, 2017, 136–144. https://doi.org/10.1109/CVPRW.2017.151
14. J. H. Yu, Z. Lin, J. M. Yang, X. H. Shen, X. Lu, T. Huang, Free-form image inpainting with gated convolution, *2019 IEEE/CVF International Conference on Computer Vision (ICCV)*, Seoul, Korea (South), 2019, 4470–4479. lhttps://doi.org/10.1109/ICCV.2019.00457
15. S. Nah, T. H. Kim, K. M. Lee, Deep multi-scale convolutional neural network for dynamic scene deblurring, *2017 IEEE Conference on Computer Vision and Pattern Recognition (CVPR)*, Honolulu, HI, USA, 2017, 257–265. https://doi.org/10.1109/CVPR.2017.35
16. T. Garber, T. Tirer, Image restoration by denoising diffusion models with iteratively preconditioned guidance, *2024 IEEE/CVF Conference on Computer Vision and Pattern Recognition (CVPR)*, Seattle, WA, USA, 2024, 25245–25254. https://doi.org/10.1109/CVPR52733.2024.02385
17. D. H. Zhang, X. Y. Hao, D. C. Wang, C. B. Qin, B. Zhao, L. L. Liang, et al., An efficient lightweight convolutional neural network for industrial surface defect detection, *Artif. Intell. Rev.*, **56** (2023), 10651–10677. https://doi.org/10.1007/s10462-023-10438-y
18. D. H. Zhang, C. C. Yu, Z. Li, C. B. Qin, R. X. Xia, A Lightweight network enhanced by attention-guided cross-scale interaction for underwater object detection, *Appl. Soft Comput.*, **184** (2025), 113811. https://doi.org/10.1016/j.asoc.2025.113811
19. C. B. Qin, X. T. Ran, D. H. Zhang, Unsupervised image stitching based on generative adversarial networks and feature frequency awareness algorithm, *Appl. Soft Comput.*, **183** (2025), 113466. https://doi.org/10.1016/j.asoc.2025.113466

20. D. H. Zhang, Y. C. Wang, L. Meng, J. Y. Yan, C. B. Qin, Adaptive critic design for safety-optimal FTC of unknown nonlinear systems with asymmetric constrained-input, *ISA T.*, **155** (2024), 309–318. https://doi.org/10.1016/j.isatra.2024.09.018

21. Y. W. Zhang, B. Zhao, D. R. Liu, Distributed optimal containment control of wheeled mobile robots via adaptive dynamic programming, *IEEE Transactions on Systems, Man, and Cybernetics: Systems*, **55** (2025), 5876–5886. https://doi.org/10.1109/TSMC.2025.3573738

22. D. H. Zhang, Q. S. Yuan, L. Meng, R. X. Xia, W. Liu, C. B. Qin, Reinforcement learning for single-agent to multi-agent systems: from basic theory to industrial application progress, a Survey, *Artif. Intell. Rev.*, (2025). https://doi.org/10.1007/s10462-025-11439-9

23. C. B. Qin, M. Y. Pang, Z. W. Wang, S. Y. Hou, D. H. Zhang, Observer based fault tolerant control design for saturated nonlinear systems with full state constraints via a novel event-triggered mechanism, *Eng. Appl. Artif. Intell.*, **161** (2025), 112221. https://doi.org/10.1016/j.engappai.2025.112221

24. O. Kupyn, T. Martyniuk, J. R. Wu, Z. Y. Wang, DeblurGAN-v2: Deblurring (orders-of-magnitude) faster and better, *2019 IEEE/CVF International Conference on Computer Vision (ICCV)*, Seoul, Korea (South), 2019, 8877–8886. https://doi.org/10.1109/ICCV.2019.00897

25. C. Ledig, L. Theis, F. Huszár, J. Caballero, A. Cunningham, A. Acosta, Photo-realistic single image super-resolution using a generative adversarial network, *2017 IEEE Conference on Computer Vision and Pattern Recognition (CVPR)*, Honolulu, HI, USA, 2017, 105–114. https://doi.org/10.1109/CVPR.2017.19

26. K. C. K. Chan, X. Y. Xu, X. T. Wang, J. W. Gu, C. C. Loy, GLEAN: Generative latent bank for image super-resolution and beyond, *IEEE T. Pattern Anal.*, **45** (2023), 3154–3168. https://doi.org/10.1109/TPAMI.2022.3186715

27. X. T. Wang, K. Yu, S. X. Wu, J. J. Gu, Y. H. Liu, C. Dong, et al., ESRGAN: Enhanced super-resolution generative adversarial networks, *Computer Vision–ECCV 2018 Workshops*, Cham: Springer, 2018, 63–79. https://doi.org/10.1007/978-3-030-11021-5_5

28. A. Lugmayr, M. Danelljan, L. V. Gool, R. Timofte, SRFlow: Learning the super-resolution space with normalizing flow, *Computer Vision–ECCV 2020)*, Cham: Springer, 2020, 715–732. https://doi.org/10.1007/978-3-030-58558-7_42

29. J. Ho, A. Jain, P. Abbeel, Denoising diffusion probabilistic models, *Advances in Neural Information Processing Systems*, **33** (2020), 6840–6851.

30. P. Osuna-Vargas, M. H. Wehrheim, L. Zinz, J. Rahm, A. Balakrishnan, A. Kaminer, et al., Denoising diffusion models for high-resolution microscopy image restoration, *2025 IEEE/CVF Winter Conference on Applications of Computer Vision (WACV)*, Tucson, AZ, USA, 2025, 4320–4330. https://doi.org/10.1109/WACV61041.2025.00424

31. M. W. Jian, R. Wang, X. Y. Yu, F. Xu, H. Yu, K. M. Lam, UniFRD: A unified method for facial image restoration based on diffusion probabilistic model, *IEEE T. Circ. Syst. Vid.*, **34** (2024), 13494–13506. https://doi.org/10.1109/TCSVT.2024.3450493

32. C. S. Dong, H. Z. Fu, A. L. He, T. Li, B. Pan, Z. N. Shi, et al., Resfusion: Denoising diffusion probabilistic models for image restoration based on prior residual noise, *Advances in Neural Information Processing Systems*, **37** (2024), 130664–130693. https://doi.org/10.52202/079017-4153

33. B. Fei, Y. X. Li, W. D. Yang, H. J. Gao, J. Y. Xu, L. P. Ma, et al., A diffusion model for universal medical image enhancement, *Commun. Med.*, **5** (2025), 294. https://doi.org/10.1038/s43856-025-00998-1

34. B. Kawar, M. Elad, S. Ermon, J. Song, Denoising diffusion restoration models, *Adv. Neural Inf. Process. Syst.*, **35** (2022), 23593–23606. https://doi.org/10.48550/arXiv.2201.11793

35. W. T. Xu, J. B. Jiao, Revisiting implicit neural representations in low-level vision, (2023), arXiv:2304.10250. https://doi.org/10.48550/arXiv.2304.10250

36. V. Sitzmann, J. Martel, A. Bergman, D. Lindell, G. Wetzstein, Implicit neural representations with periodic activation functions, *Advances in Neural Information Processing Systems*, **33** (2020), 7462–7473.

37. D. Jayasundara, H. Zhao, D. Labate, V. M. Patel, MIRE: Matched implicit neural representations, *2025 IEEE/CVF Conference on Computer Vision and Pattern Recognition (CVPR)*, Nashville, TN, USA, 2025, 8279–8288. https://doi.org/10.1109/CVPR52734.2025.00775

38. S. L. Hauser, J. Brosig, B. Murthy, A. Attardo, Implicit neural representations in light microscopy, *Biomed. Opt. Express*, **15** (2024), 2175–2186. https://doi.org/10.1364/BOE.515517

39. Z. X. Huang, S. M. Erfani, S. Y. Lu, M. M. Gong, Efficient neural implicit representation for 3D human reconstruction, *Pattern Recogn.*, **156** (2024), 110758. https://doi.org/10.1016/j.patcog.2024.110758

40. X. Lin, J. T. Yue, K. C. K. Chan, L. Qi, C. Ren, J. S. Pan, et al., Multi-task image restoration guided by robust DINO features, (2023), arXiv:2312.01677. https://doi.org/10.48550/arXiv.2312.01677

41. B. Y. Li, H. Y. Zhao, W. X. Wang, P. Hu, Y. B. Gou, X. Peng, MAIR: A locality- and continuity-preserving mamba for image restoration, *2025 IEEE/CVF Conference on Computer Vision and Pattern Recognition (CVPR)*, Nashville, TN, USA, 2025, 7491–7501. https://doi.org/10.1109/CVPR52734.2025.00702

42. W. Y. Bian, A. Jang, F. Liu, Multi-task magnetic resonance imaging reconstruction using meta-learning, *Magn. Reson. Imaging*, **116** (2025), 110278. https://doi.org/10.1016/j.mri.2024.110278

43. J. Y. Liang, J. Z. Cao, G. L. Sun, K. Zhang, L. V. Gool, R. Timofte, SwinIR: Image restoration using swin transformer, *2021 IEEE/CVF International Conference on Computer Vision Workshops (ICCVW)*, Montreal, BC, Canada, 2021, 1833–1844. https://doi.org/10.1109/ICCVW54120.2021.00210

44. A. Molaei, A. Aminimehr, A. Tavakoli, A. Kazerouni, B. Azad, R. Azad, et al., Implicit neural representation in medical imaging: A comparative survey, *2023 IEEE/CVF International Conference on Computer Vision Workshops (ICCVW)*, Paris, France, 2023, 2373–2383. https://doi.org/10.1109/ICCVW60793.2023.00252

45. Y. J. Zhu, Y. Y. Liu, Y. H. Zhang, D. Liang, Implicit neural representation for medical image reconstruction, *Phys. Med. Biol.*, **70** (2025), 12TR01. https://doi.org/10.1088/1361-6560/addfa5

46. H. Chen, W. C. Zhao, T. F. Xu, G. K. Shi, S. Y. Zhou, P. F. Liu, et al., Spectral-wise implicit neural representation for hyperspectral image reconstruction, *IEEE T. Circ. Syst. Vid.*, **34** (2024), 3714–3727. https://doi.org/10.1109/TCSVT.2023.3318366

47. J. Sun, W. S. Wang, Adaptive selection of shape parameters for MQRBF in arbitrary scattered data: enhancing finite difference solutions for complex PDEs, *Comp. Appl. Math.*, **43** (2024), 449. https://doi.org/10.1007/s40314-024-02970-6

48. B. Y. Li, X. Liu, P. Hu, Z. Q. Wu, J. C. Lv, X. Peng, All-in-one image restoration for unknown corruption, *2022 IEEE/CVF Conference on Computer Vision and Pattern Recognition (CVPR)*, New Orleans, LA, USA, 2022, 17431–17441. https://doi.org/10.1109/CVPR52688.2022.01693

49. Z. D. Wang, X. D. Cun, J. M. Bao, W. G. Zhou, J. Z. Liu, H. Q. Li, Uformer: A general U-shaped transformer for image restoration, *2022 IEEE/CVF Conference on Computer Vision and Pattern Recognition (CVPR)*, New Orleans, LA, USA, 2022, 17662–17672. https://doi.org/10.1109/CVPR52688.2022.01716

AIMS Press